Mechatronics 22 (2012) 282–294

Contents lists available at SciVerse ScienceDirect

Mechatronics

journal homepage: www.elsevier.com/locate/mechatronics

Dynamics, load balancing, and modal control of piezoelectric tube actuators

J.R. van Hulzen [a,*], G. Schitter [b], P.M.J. Van den Hof [a], J. van Eijk [c]

[a] Delft Center for Systems and Control, Delft University of Technology, Mekelweg 2, 2628 CD Delft, The Netherlands
[b] Automation and Control Institute, Vienna University of Technology, Gusshausstrasse 27-29, 1040 Vienna, Austria
[c] Department of Precision and Microsystems Engineering, Delft University of Technology, Mekelweg 2, 2628 CD Delft, The Netherlands

ARTICLE INFO

Article history:
Available online 25 November 2011

Keywords:
Modal control
Mode analysis
Mechanical properties
Finite element analysis
Model based control
Microscopes

ABSTRACT

In piezoelectric positioning systems the achievable bandwidth is often limited by weakly damped resonant modes. System performance may be improved by avoiding the excitation of these modes. If sufficient mechanical damping is present this can be done by shifting resonant modes towards anti-resonant modes through manipulation of the mechanical boundary conditions. In a second approach the anti-resonances may be shifted towards the resonances by the application of modal actuation. Using this method the excitation of the second and higher order modes can be avoided by adjusting the distribution of actuation forces. This paper investigates and compares the application of modal control techniques in systems that are based on piezoelectric tube actuators such as atomic force microscopes.

1. Introduction

Piezoelectric actuators are used in applications where high precision positioning is required over a relatively short range. A typical example of such an application is the atomic force microscope (AFM) [1]. In AFM systems, the sample-probe interaction is regulated by feedback control to avoid sample damage during imaging. A common problem in the design of systems such as AFMs is the excitation of resonant modes associated with the mechanical parts of the system. This is especially true for resonant modes with natural frequencies which are close to the bandwidth of the feedback control system. Possible solutions to this problem are based on avoiding excitation of these modes by adapting the control system architecture [2] or by increasing the number of sensors and actuators to enable individual control of resonant modes [3,4]. This last approach is a form of distributed control and is commonly referred to as modal actuation. The technique was successfully applied in piezoelectric actuated systems by shaping the drive electrodes by etching [5], by application of porous electrodes or electrodes with a honeycomb motif [6,7]. An alternative form of modal actuation is based on arrays of individual piezoelectric transducers and has been reported in [8,9].

A key aspect of modal actuation is that the response to external excitation is changed without altering the natural modes or the natural frequencies. This is achieved by changing the distribution of forces applied to the system. The design of a modal actuator can be based directly on the mode shapes. Implementation of modal actuation is difficult if the mode shapes are very complex, if the flexible structure can only be actuated partially or in cases where the dynamics are uncertain due to changing load conditions or by the introduction of flexible loads. In an alternative approach [10], the natural modes are shifted towards the anti-resonances by manipulation of the mechanical boundary conditions. Sufficiently damped natural modes which are close to an anti-resonance will appear less pronounced reducing their impact on the design of the feedback control loop.

This paper investigates the application of both forms of modal actuation to positioning systems where the piezoelectric tube actuator is the main flexible component. The objective is to determine which modes are important to the realization of the position control objective and to show that these modes can be controlled through modal actuation. The actuator used to demonstrate the principle is based on sectioned rather than shaped electrodes which increases design flexibility and enables in situ adaptation to changing load conditions. Using sectioned electrodes, the distribution of the electric field may be tuned by varying the voltages supplied to each section.

The paper is organized as follows. In Section 2, piezoelectric actuation is introduced and the formulation of models of piezoelectric tube actuators based on shell-theory as well as models derived by finite element analysis (FEA) are presented. In Section 3, manipulation of the dynamical properties using mechanical boundary conditions is discussed. Modal actuation is described in Section 4. In Section 5, the limitations of modal control are investigated. Experimental verification of modal control techniques is

* Corresponding author. Tel.: +31 627055794.
E-mail addresses: j.r.vanhulzen@tudelft.nl, jr.v.hulzen@nlda.nl (J.R. van Hulzen), schitter@acin.tuwien.ac.at (G. Schitter), p.m.j.vandenhof@tudelft.nl (P.M.J. Van den Hof), J.vanEijk@tudelft.nl (J. van Eijk).

0957-4158/$ - see front matter © 2011 Elsevier Ltd. All rights reserved.
doi:10.1016/j.mechatronics.2011.10.003

presented in Section 6. Finally, concluding remarks are given in Section 7.

2. Piezoelectric actuation

A piezoelectric actuator consists of a stiff ceramic material which expands in the presence of an electric field. In [10,11] dynamic models of piezoelectric actuators based on Euler–Bernoulli beam theory are proposed. In cases where piezoelectric tube actuators are applied, beam type models need to be extended to incorporate extensional, flexural and due to the curvature of the tube, coupled flexural-extensional deformation.

Models of piezoelectric tube actuators based on shell theory (see [12,13] for an overview) incorporate both flexural and extensional deformations and are capable of predicting the coupling between axial and radial deformation. However, due to the complex nature of models based on shell theory, closed form solutions exist only in very simple cases and numerical approximations are often necessary. Therefore, models based on shell theory are used to develop the underlying principle of modal actuation and the effectiveness of the technique is demonstrated in a specific case using a numerical approximation based on finite element formulation. Finite element models of piezoelectric tube actuators have been proposed in [14,15]. Using this framework, the application of modal control through variation of the load as well as the application of modal control based on sectioned electrodes is investigated using a case study of a high speed AFM.

2.1. Axial vibration of a piezoelectric tube scanner

The vertical axis of a tube scanner is modeled under the assumption that the piezoelectric tube actuator is a perfect, thin walled cylindrical shell with uniform electrodes. The actuator is assumed to be bonded to a flat base and it is assumed that the load has the form of a flat disk of radius r_d and thickness h_d which is mounted on the free end of the actuator in such a way that the centrelines of actuator and disk coincide. The length of the actuator is denoted as L, the radius of the cylinder mid-surface as R and the area of the lateral cross section of the cylinder is denoted as A. In the shell theory model presented below it is assumed that the thickness of the cylinder wall h is less than 10% of the mid-surface radius R and that the deformations of the shell are small compared to its dimensions. It is assumed that the expansion of the piezoelectric material in the polarization direction is negligible when compared to axial deformation due to bending and stretching and radial deformation due to hoop strain. The piezoelectric material is assumed to be orthotropic with respect to the polarization axis which is perpendicular to the cylinder surface. However, under the shell-theory assumptions, the material can be considered isotropic with material constants defined as modulus of elasticity E, Poisson's ratio ν[1] and density ρ. It is assumed that actuation due to the application of an electric field results in an axisymmetrical deformation of the actuator. Deformations in circumferential direction such as torsion and bending are neglected. Axial and radial deformation are denoted by $u(z,t)$ and $w(z,t)$. Deformations $u(z,t)$ and $w(z,t)$ are assumed to be uniform in circumferential direction and vary only with time and the vertical axis (z-axis) position. Partial derivatives of u and w with respect to spatial variable z and time variable t are denoted as $'(z,t)$ and $\dot{}(z,t)$. Using Flügge shell theory [16,17] it follows that the strain in axial and radial direction ϵ_α and ϵ_β may be related to mid-surface displacement u and w by:

$$\epsilon_\alpha = u' - rw'',$$

$$\epsilon_\beta = \frac{w}{R+r},$$

where the term $-zw''$ is included to take mid-surface bending into account, see Fig. 1. To find the stresses σ_α and σ_β the strain variables ϵ_α and ϵ_β can be inserted into Hooke's law to find:

$$\sigma_\alpha = \frac{E}{1-\nu^2}(\epsilon_\alpha + \nu\epsilon_\beta),$$

$$\sigma_\beta = \frac{E}{1-\nu^2}(\epsilon_\beta + \nu\epsilon_\alpha).$$

Integration of the product of stress and strain over the volume of the cylindrical shell yields the expression for strain energy

$$V = \frac{E}{2(1-\nu^2)}\int_\Omega \epsilon_\alpha^2 + \epsilon_\beta^2 + 2\nu\epsilon_\alpha\epsilon_\beta d\Omega.$$

Integration over a shell element $d\Omega$ may be expressed in terms of the coordinates r,θ and z which yields $d\Omega = (R+r)/R\ dr\ d\theta dz$, see also Fig. 1a. In the axisymmetric case considered here, the integration over θ is equivalent to multiplication with the circumference of the circular cylindrical mid-surface given by $2\pi R$. Integration over the thickness of the shell yields

$$\begin{aligned} V &= \frac{E2\pi R}{2(1-\nu^2)}\int_0^L\int_{-h/2}^{h/2}\left\{(u'-rw'')^2 + \left(\frac{w}{R+r}\right)^2 \right.\\ &\quad \left. +2\nu(u'-rw'')\left(\frac{w}{R+r}\right)\right\}\frac{R+r}{R}drdz \\ &= \frac{EA}{2(1-\nu^2)}\int_0^L\left\{(u')^2 - 2\frac{h^2}{12R}u'w'' + \frac{h^2}{12}(w'')^2 + \frac{w^2}{R^2} + \frac{h^2}{12R^4}w^2 + 2\frac{\nu}{R}u'w\right\}dz \end{aligned}$$

where $A = 2\pi Rh$ is the area of the longitudinal (axial) cross section of the cylinder. For thin shells the expression for stored kinetic energy during elastic deformation is given by

$$T = \frac{1}{2}\rho A\int_0^L \dot{u}^2 + \dot{w}^2 dz + \frac{1}{2}m_l\dot{u}(L,t),$$

where m_l is the mass of the disk load. Using Hamilton's principle it follows that

$$\delta\int_{t_1}^{t_2}(T-V)dt = \int_{t_1}^{t_2}\int_0^L \delta\widehat{L}\,dz\,dt \quad \delta u(z,t) = \delta w(z,t) = 0,$$
$$0 \leqslant z \leqslant L,\ t = t_1, t_2,$$

where δ denotes the variation and $\widehat{L}$ is the Lagrangian density. Using integration by parts to eliminate variations of derivatives of $u(z,t)$ and $w(z,t)$ with respect to z and t it follows that:

$$\int_{t_1}^{t_2}\left\{\int_0^L\left[\frac{\partial}{\partial z}\left(\frac{\partial\widehat{L}}{\partial u'}\right) + \frac{\partial}{\partial t}\left(\frac{\partial\widehat{L}}{\partial\dot{u}}\right)\right]\delta u\,dz - \left[\frac{\partial\widehat{L}}{\partial u'}\right]\delta u\ \Big|_0^L\right\}dt = 0$$

$$\int_{t_1}^{t_2}\left\{\int_0^L\left[\frac{\partial\widehat{L}}{\partial w} - \frac{\partial}{\partial z}\left(\frac{\partial\widehat{L}}{\partial w'}\right) + \frac{\partial^2}{\partial z^2}\left(\frac{\partial\widehat{L}}{\partial w''}\right) - \frac{\partial}{\partial t}\left(\frac{\partial\widehat{L}}{\partial\dot{w}}\right)\right]\delta w\,dz\right\}dt = 0,$$

where it has been assumed that $\delta w(z,t) = \delta w'(z,t) = 0$ at $z = 0$ and $z = L$ due to the fact that the actuator is rigidly connected to the base and to the load which is assumed to be rigid.

$$\frac{E}{1-\nu^2}\left[u''(z,t) - \frac{h^2}{12R}w'''(z,t) + \frac{\nu}{R}w'(z,t)\right] = \rho\ddot{u}(z,t) \tag{1}$$

[1] Using material data supplied by manufactures, the elasticity modulus E may be derived from $E = (1-\nu^2)(c_{11}^E + e_{31}^2/\varepsilon_{33})$ and Poisson's ratio ν from $\nu = (c_{12}^E + e_{31}^2/\varepsilon_{33})/(c_{11}^E + e_{31}^2/\varepsilon_{33})$ when using the charge boundary condition in an open-circuit condition.

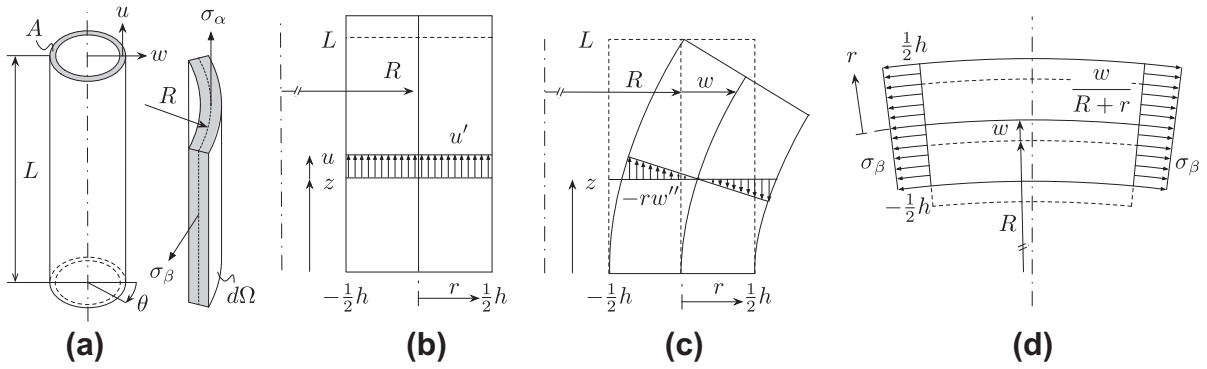

Fig. 1. Piezoelectric tube actuator with shell element (a) and strain as a function of mid-surface deformation with deformations due to longitudinal stretching (b), due to bending (c) and due to radial expansion (d).

$$\frac{E}{1-\nu^2}\left[\frac{h^2}{12R}u'''(z,t)-\frac{h^2}{12}w^{IV}(z,t)\right] - \frac{E}{1-\nu^2}\left[\frac{\nu}{R}u'(z,t)+\frac{1}{R^2}w(z,t)+\frac{h^2}{12R^4}w(z,t)\right] = \rho\ddot{w}(z,t), \tag{2}$$

with $0 < z < L$. The boundary conditions imposed on (1) and (2) depend on the displacements as well as the tensile, bending and shearing forces at the interfaces and are formulated as conditions on the solutions $u(z,t)$ and $w(z,t)$. The boundary conditions on $u(z,t)$ are

$$u(z,t)=0,\ z=0;\quad -\frac{EA}{1-\nu^2}\left[u'(z,t)-\frac{h^2}{12R}w''(z,t)\right]=m_l\ddot{u}(z,t), z=L. \tag{3}$$

The boundary conditions on $w(z,t)$ are defined by assuming a rigid connection between tube and load. This results in:

$$w(z,t)=0,\quad w'(z,t)=0 \text{ for } z=0, z=L. \tag{4}$$

Under the assumption that the system executes synchronous motion, the solutions of (1) and (2) can be written as:

$$u_i(z,t)=U_i(z)\cos(\omega_i t-\alpha_i),\ w_i(z,t)=W_i(z)\cos(\omega_i t-\alpha_i), \tag{5}$$

where $u_i(z,t)$ and $w_i(z,t)$ are the natural motions with $U_i(z)$ and $W_i(z)$ as the mode shapes of the natural modes and ω_i as the natural frequencies which are obtained by solving the differential Eigenvalue problem. Using (5), Eqs. (1) and (2) transform into:

$$-U_i''(z)-\frac{\nu}{R}W_i'(z)+\frac{h^2}{12R}W_i'''(z)=\frac{(1-\nu^2)\rho}{E}\omega_i^2U_i(z) \tag{6}$$

$$\frac{\nu}{R}U_i'(z)-\frac{h^2}{12R}U_i'''(z)+\frac{W_i(z)}{R^2}+\frac{h^2W_i(z)}{12R^4}+\frac{h^2}{12}W_i^{IV}(z)=\frac{(1-\nu^2)\rho}{E}\omega_i^2W_i(z) \tag{7}$$

for $0 < z < L$ and

$$U_i(z)=0 \text{ for } z=0,\quad \frac{EA}{1-\nu^2}\left[U_i'(z)-\frac{h^2}{12R}W_i''(z)\right]=\omega_i^2m_lU_i(z) \text{ for } z=L,$$

$$W_i(z)=0, W_i'(z)=0 \text{ for } z=0 \text{ and } z=L.$$

To show that the separate modes at frequency ω_i can be excited independently it is necessary to derive the orthogonality conditions.

2.2. Orthogonality

To derive the orthogonality conditions, two solutions $U_a(z)$, $W_a(z)$ and $U_b(z)$, $W_b(z)$ satisfying (6) and (7) are compared. Inserting the solution $U_a(z)$, $W_a(z)$ into (6), multiplying the result with $U_b(z)$ and integrating the result over z yields:

$$-\int_0^L U_b(z)U_a''(z)dz-\frac{\nu}{R}\int_0^L U_b(z)W_a'(z)dz+\frac{h^2}{12R}\int_0^L U_b(z)W_a'''(z)dz = \frac{(1-\nu^2)\rho}{E}\omega_a^2\int_0^L U_b(z)U_a(z)dz. \tag{8}$$

Integrating the first term of the left hand side by parts and inserting the boundary conditions yields

$$-\int_0^L U_b(z)U_a''(z)dz=-\frac{h^2}{12R}U_b(L)W_a''(L)-\omega_a^2m_l\frac{(1-\nu^2)}{EA}U_b(L)U_a(L)+\int_0^L U_b'(z)U_a'(z)dz.$$

Integrating the second term of (8) by parts and inserting the boundary condtions yields

$$-\frac{\nu}{R}\int_0^L U_b(z)W_a'(z)dz=\frac{\nu}{R}\int_0^L U_b'(z)W_a(z)dz.$$

Finally, by using integration by parts three times and inserting the boundary conditions the third term of (8) is transformed into

$$\frac{h^2}{12R}\int_0^L U_b(z)W_a'''(z)dz=\frac{h^2}{12R}U_b(L)W_a''(L)-\frac{h^2}{12R}\int_0^L W_a(z)U_b'''(z)dz.$$

By inserting the results back into (8) we end up with

$$\int_0^L U_b'(z)U_a'(z)dz+\frac{\nu}{R}\int_0^L U_b'(z)W_a(z)dz-\frac{h^2}{12R}\int_0^L W_a(z)U_b'''(z)dz = \omega_a^2\frac{(1-\nu^2)}{EA}\left\{\rho A\int_0^L U_b(z)U_a(z)dz+m_lU_b(L)U_a(L)\right\}. \tag{9}$$

Using (6) with $i = b$, multiplying the result with $U_a(z)$ and repeating the same steps a very similar result is obtained. Subtracting this result from (9) yields

$$\frac{v}{R}\int_0^L \left[U_b'(z)W_a(z) - U_a'(z)W_b(z)\right]dz + \frac{h^2}{12R} \times \int_0^L \left[W_b(z)U_a'''(z) - W_a(z)U_b'''(z)\right]dz = \left(\omega_a^2 - \omega_b^2\right)\frac{(1-\nu^2)}{EA}\left\{\rho A\int_0^L U_b(z)U_a(z)dz + m_l U_b(L)U_a(L)\right\}. \quad (10)$$

Inserting the solution $U_a(z)$, $W_a(z)$ into (7), multiplying the result with $W_b(z)$ and integrating the result over x yields

$$\frac{v}{R}\int_0^L W_b(z)U_a'(z)dz - \frac{h^2}{12R}\int_0^L W_b(z)U_a'''(z)dz + \frac{1}{R^2}\int_0^L W_b(z)W_a(z)dz + \frac{h^2}{12R^4}\int_0^L W_b(z)W_a(z)dz + \frac{h^2}{12}\int_0^L W_b(z)W_a^{IV}(z)dz = \frac{(1-\nu^2)\rho}{E}\omega_a^2\int_0^L W_b(z)W_a(z)dz. \quad (11)$$

Integrating the last term of the left hand side by parts and applying the boundary conditions yields

$$\frac{h^2}{12}\int_0^L W_b(z)W_a^{IV}(z)dz = \frac{h^2}{12}\int_0^L W_a(z)W_b^{IV}(z)dz.$$

Again, using (7) with $i = b$, multiplying the result with $U_a(z)$ and repeating the same steps a similar result is obtained. Subtracting this result from (11) yields

$$\frac{v}{R}\int_0^L \left[W_b(z)U_a'(z) - W_a(z)U_b'(z)\right]dz + \frac{h^2}{12R}\int_0^L \left[W_a(z)U_b'''(z) - W_b(z)U_a'''(z)\right]dz = \frac{(1-\nu^2)\rho}{E}\left(\omega_a^2 - \omega_b^2\right)\int_0^L W_b(z)W_a(z)dz. \quad (12)$$

Then by adding (12) to (10) it follows that:

$$\left(\omega_a^2 - \omega_b^2\right)\left\{\rho A\int_0^L \left[U_b(z)U_a(z) + W_b(z)W_a(z)\right]dz + m_l U_b(L)U_a(L)\right\} = 0.$$

This last expression leads to the orthogonality condition:

$$\rho A\int_0^L \left[U_b(z)U_a(z) + W_b(z)W_a(z)\right]dz + m_l U_b(L)U_a(L) = \mu_a\delta_{ab},$$

where δ_{ab} and μ_a are defined as the Kronecker delta function and a positive constant commonly referred to as the modal mass. These results are similar to the results found in [18,17] but include the influence of the attached rigid mass. If the radial deformation is neglected the orthogonality condition is identical to that of a Euler–Bernoulli beam loaded by a rigid mass [19]. The modal mass μ_a can be determined with:

$$\mu_a = \rho A\int_0^L \left[U_a^2(z) + W_a^2(z)\right]dz + m_l U_a^2(L).$$

The complementary orthogonality condition can be found in a similar fashion.

$$\int_0^L U_b'(z)U_a'(z)dz + \frac{h^2}{12R}\int_0^L U_b(z)W_a'''(z) - W_b(z)U_a'''(z)dz - \frac{h^2}{12R}U_b(L)W_a''(L) + \frac{v}{R}\int_0^L W_b(z)U_a'(z)dz - \frac{v}{R}\int_0^L U_b(z)W_a'(z)dz + \frac{12R^2+h^2}{12R^4}\int_0^L W_b(z)W_a(z)dz + \frac{h^2}{12}\int_0^L W_b(z)W_a^{IV}(z)dz = \frac{(1-\nu^2)}{EA}\omega_a^2\mu_a\delta_{ab}.$$

Using the orthogonality conditions it can be shown that the resonant modes of the system are independent of each other.

2.3. Response to external excitation

To calculate the response of the system to excitation by a voltage applied to the electrodes of the system (1) and (2) are extended to:

$$\frac{E}{1-\nu^2}\left[u''(z,t) - \frac{h^2}{12R}w'''(z,t) + \frac{v}{R}w'(z,t)\right] + f_u(z,t) = \rho\ddot{u}(z,t) \quad (13)$$

$$\frac{E}{1-\nu^2}\left[\frac{h^2}{12R}u'''(z,t) - \frac{h^2}{12}w^{IV}(z,t) - \frac{v}{R}u'(z,t) - \frac{w(z,t)}{R^2} - \frac{h^2}{12R^4}w(z,t)\right] + f_w(z,t) = \rho\ddot{w}(z,t), \quad (14)$$

where $f_u(z,t)$, $f_w(z,t)$ are the net-forces generated by the piezoelectric effect per unit length of the piezo. The piezoelectric effect causes the actuator to expand axially as well as radially. The radial expansion is assumed to be caused by the increase of the circumference of the tube. The expansion of the material itself, i.e. the increase in wall thickness h is assumed to be negligible. With these assumptions $f_u(z,t)$, $f_w(z,t)$ are given by:

$$f_u(z,t) = 2\pi\frac{A}{L}\frac{e_{31}}{\ln\left(\frac{R+h/2}{R-h/2}\right)}F(z)V(t),$$

$$f_w(z,t) = 2\pi\frac{A}{R}\frac{e_{31}}{\ln\left(\frac{R+h/2}{R-h/2}\right)}F(z)V(t),$$

where $F(z)$ is a shaping function. In the case of a modal actuator based on a single shaped, porous or honeycombed electrode, the shaping function $F(z)$ is a continuous function and the product of $F(z)$ and $V(t)$ denotes the voltage level at coordinate z. In the case of a modal actuator based on a sectioned electrode, the layout shown in Fig. 2 is used. In this case the voltage levels are uniform within a section and $F(z)$ has the form:

$$F(z) = \sum_{j=1}^{n+1} g_j\left(\delta(z - z_j) - \delta(z - z_{j+1})\right), \quad (15)$$

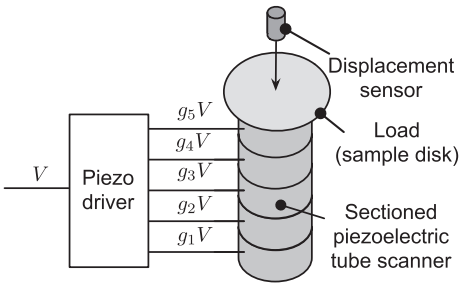

Fig. 2. Sectioned modal actuator with an outer electrode divided into five sections of uniform length, a load in the form of a sample disk and a sensor measuring the vertical displacement of the load.

where δ is a dirac function with the property that $\int_{-\infty}^{\infty}\delta(z)dz = 1$ and $\delta(z - z_0) = 0$ for $z \neq z_0$. In (15), n denotes the number of sections and z_j is the coordinate of the lower boundary of a section. The voltage levels on each section are determined by a section gain g_j. Using the orthogonality property, the axial and radial deformations can be written as:

$$u(z,t) = \sum_{i=1}^{\infty} U_i(z)q_i(t), \tag{16}$$

$$w(z,t) = \sum_{i=1}^{\infty} W_i(z)q_i(t), \tag{17}$$

where $U_i(z)$, $W_i(z)$ are modeshapes associated with the resonant mode i with Eigen frequency ω_i and $q_i(t)$ are generalized coordinates dependent on time. Using the orthogonality conditions (13) and (14) are transformed into:

$$\ddot{q}_i(t) + \omega_i^2 q_i(t) = \mu_i^{-1}\int_0^L (U_i(z) + W_i(z))f(z,t)dz. \tag{18}$$

Without loss of generality we can assume that the voltage applied to the electrodes is given by

$$V(t) = V\cos\omega t. \tag{19}$$

Inserting (19) into (18) and the resulting expression into (16) yields

$$u(z,t) = \sum_{i=1}^{\infty} \frac{\int_0^L (U_i(z) + W_i(z))F(z)dz}{\mu_i(\omega_i^2 - \omega^2)} U_i(z)\cos\omega t.$$

Using (15) $u(z,t)$ changes into

$$u(z,t) = \sum_{i=1}^{\infty} \frac{\sum_{j=1}^{n+1} g_j\{U_i(z-z_j) + W_i(z-z_j) - U_i(z-z_{j+1}) - W_i(z-z_{j+1})\}}{\mu_i(\omega_i^2 - \omega^2)} U_i(z) \times \cos\omega t.$$

Finally, the transfer function from voltage to extension at $z = L$ as a function of ω is

$$H(\omega) = \sum_{i=1}^{\infty} \frac{\sum_{j=1}^{n+1} g_j\{U_i(z-z_j) + W_i(z-z_j) - U_i(z-z_{j+1}) - W_i(z-z_{j+1})\}}{\mu_i(\omega_i^2 - \omega^2)} U_i(L).$$

To calculate the transfer function for a given set of gains $g_1,\ldots,g_n$ it is necessary to calculate the solutions of (1) and (2) taking into account the boundary conditions (3) and (4). This can be done if $U(z)$ and $W(z)$ are known. In cases with simple boundary conditions, closed form solutions can be obtained. However in most cases $U(z)$ and $W(z)$ are derived numerically either by constructing them from a set of trial functions using the Ritz-method or by discretization using the finite-element approach.

2.4. Solutions based on the Ritz-method

Using the strain- and kinetic-energy expressions in combination with the Ritz-procedure, an approximate solution $U(z)$ and $W(z)$ can be constructed by optimization over a set of trail functions. In literature various trial functions have been suggested [20–22]. The trial functions adopted here are derived from fixed-free Euler–Bernoulli beams in bending. The boundary condition defined by the load is taken into account by expanding the set of trial functions using a set of functions defined for fixed–fixed Euler–Bernoulli beams in bending. Using this approach the solution for $U(z)$ is allowed to have a non-zero slope at $z = L$. To avoid numerical problems an alternative formulation suggested in [23] was used. The functions defining the fixed-free set are given by:

$$\phi_i(z) = \cos\frac{\lambda_i z}{L} + C2_i\sin\frac{\lambda_i z}{L} + C3_i e^{-\lambda_i\frac{z}{L}} + C4_i e^{-\lambda_i\left(1-\frac{z}{L}\right)},$$

with $C2_i$, $C3_i$, $C4_i$ and γ_i are defined as:

$$C2_i = -\frac{1+(-1)^i e^{-\gamma_i}}{1-(-1)^i e^{-\gamma_i}}, \quad C3_i = -\frac{1}{1-(-1)^i e^{-\gamma_i}},$$

$$C4_i = -\frac{(-1)^i}{1-(-1)^i e^{-\gamma_i}}, \quad \cos\gamma_i + \frac{2e^{-\gamma_i}}{1+e^{-2\gamma_i}} = 0.$$

The functions defined for the fixed–fixed beam in bending are defined as:

$$\psi_i(z) = \cos\frac{\zeta_i z}{L} + D_2\sin\frac{\zeta_i z}{L} + D_3 e^{-\zeta_i\frac{z}{L}} + D_4 e^{-\zeta_i\left(1-\frac{z}{L}\right)},$$

where $D2_i$, $D3_i$, $D4_i$ and ζ_i are defined as:

$$D2_i = -\frac{1+(-1)^i e^{-\zeta_i}}{1-(-1)^i e^{-\zeta_i}}, \quad D3_i = -\frac{1}{1-(-1)^i e^{-\zeta_i}},$$

$$D4_i = -\frac{(-1)^i}{1-(-1)^i e^{-\zeta_i}}, \quad \cos\zeta_i - \frac{2e^{-\zeta_i}}{1+e^{-2\zeta_i}} = 0.$$

The solutions $U(z)$ and $W(z)$ are then constructed using

$$U^{(n)}(z) = \sum_{i=1}^{n} a_i\frac{L}{\gamma_i}\frac{d\phi_i(z)}{dz} + c_i\frac{L}{\zeta_i}\frac{d\psi_i(z)}{dz},$$

$$W^{(n)}(z) = \sum_{i=1}^{n} b_i\phi_i(z) + d_i\psi_i(z).$$

The coefficients a_i, b_i, c_i and d_i are found by solving the Eigenvalue problem defined by the strain and kinetic energy expressions. To increase accuracy and numerical stability, integration of the trial functions was first carried out using the expressions found in [24,25]. Expanding the set of trail functions for more complicated cases where flexibility of the load and mount are taken into account leads to Eigenvalue problems which are numerically challenging. In this paper these cases were solved using the finite element method.

2.5. Solutions based on the finite element method

A finite element model used to describe the dynamics of the piezoelectric tube actuator and its load has been implemented using ANSYS [26]. The model is based on 8-node coupled field elements (SOLID5). To increase symmetry, the elements are arranged in a regular mapped mesh. A relatively high mesh density of 80 by 95 by 2 in axial, circumferential and radial direction has been applied to enable accurate prediction of high order modes with complex mode shapes and to avoid stiffening effects such as shear locking. In low voltage regimes, the direct and indirect piezoelectric effect can be modeled using linear the constitutive equations:

$$\begin{bmatrix}\sigma_1\\ \sigma_2\\ \sigma_3\\ \sigma_4\\ \sigma_5\\ \sigma_6\\ \mathbb{D}_1\\ \mathbb{D}_2\\ \mathbb{D}_3\end{bmatrix} = \begin{bmatrix} c_{11}^E & c_{12}^E & c_{13}^E & 0 & 0 & 0 & 0 & 0 & -e_{31}\\ c_{12}^E & s_{11}^E & s_{13}^E & 0 & 0 & 0 & 0 & 0 & -e_{31}\\ c_{13}^E & c_{13}^E & s_{33}^E & 0 & 0 & 0 & 0 & 0 & -e_{33}\\ 0 & 0 & 0 & c_{44}^E & 0 & 0 & 0 & -e_{15} & 0\\ 0 & 0 & 0 & 0 & c_{44}^E & 0 & -e_{15} & 0 & 0\\ 0 & 0 & 0 & 0 & 0 & c_{66}^E & 0 & 0 & 0\\ 0 & 0 & 0 & 0 & e_{15} & 0 & \varepsilon_{11} & 0 & 0\\ 0 & 0 & 0 & e_{15} & 0 & 0 & 0 & \varepsilon_{11} & 0\\ e_{31} & e_{31} & e_{33} & 0 & 0 & 0 & 0 & 0 & \varepsilon_{33}\end{bmatrix}\begin{bmatrix}\epsilon_1\\ \epsilon_2\\ \epsilon_3\\ \epsilon_4\\ \epsilon_5\\ \epsilon_6\\ \mathbb{E}_1\\ \mathbb{E}_2\\ \mathbb{E}_3\end{bmatrix}$$

in which σ and ϵ are the mechanical stresses and strains and $\mathbb{E}$ and $\mathbb{D}$ are the electric field strength and displacement. The anisotropic material data relating the stress and the strain given in short circuit conditions is denoted by c^E listed in Table 1. In this case the tensor notations commonly used in manufacturer data sheets are retained.

Table 1
Material data PIC151 piezoceramic.

Par	Value	Par	Value
c_{11}^E	1.076×10^{11} N/m^2	e_{31}	−9.60 N/Vm
c_{12}^E	6.312×10^{10} N/m^2	e_{33}	15.10 N/Vm
c_{13}^E	6.385×10^{10} N/m^2	e_{15}	12.00 N/Vm
c_{33}^E	1.004×10^{11} N/m^2	ε_{11}^S	9.8281×10^9
c_{44}^E	1.962×10^{10} N/m^2	ε_{33}^S	7.5261×10^9
c_{66}^E	2.224×10^{10} N/m^2	ε_{33}^T	1.8673×10^8
ρ	7.76×10^3 kg/m^3	Q	88

Rigid boundary conditions are incorporated using coupled sets of constraint equations. The mechanical degrees of freedom of nodes at the interface between the tube and mechanical ground are fixed to zero displacement. The nodes on the upper, free end of the tube are coupled by a set of constraint equations with a rigid mass element (Mass21). In the case of flexible load or base, additional bodies were included in the mesh. To reduce the number of nodes required for an accurate solution, an axisymmetric model based on the 2D elements Plane223 and Plane82 was constructed. Using this approach the models including a flexible base were formulated. Electrically, the nodes of the inner and outer electrodes are coupled. The coupling of nodes of the outer electrode can be sub divided into groups if sectioned, electrically-isolated electrodes are used. Harmonic responses are obtained by defining the voltage degree of freedom on the coupled input nodes as input degree of freedom and the displacement of the top-center of the disk is defined as the output degree of freedom.

3. Modal control by load balancing

The dynamics of the piezoelectric actuator are influenced by the presence of mechanical loads. In a well designed system this influence can be used to reduce unwanted excitation of resonant modes during feedback controlled positioning. The advantage of this reduction is that the stability and performance of the system may be extended. In AFM applications, a common type of load is a sample disk. In Fig. 3, the harmonic response of a loaded piezoelectric tube actuator with a length of 30 mm and a diameter of 10 mm is shown. The input of the system is the voltage applied to the electrodes of the piezoelectric actuator. The output is the displacement of the load evaluated at the contact point between sample and AFM probe. The sample disk is assumed to be a rigid steel disk with a radius r_d of 6 mm. Due to the rigid nature of the disk, the displacement U_z of the disk chosen as output is equal to the actuator elongation evaluated at the free end of the actuator.

To investigate the effect of a load on the dynamics of the actuator, the thickness h_d of the load is varied between 0.76 mm and 1.52 mm. The harmonic response depicted in Fig. 3 shows that the low order natural modes of a loaded actuator shift towards lower frequencies due to the increased load mass. From the results shown in Fig. 3, it can be concluded that the second mode is shifted towards the first anti-resonance which is unaffected by the presence of the load. The first natural mode shifts towards a lower frequency. This result is in accordance with Euler–Bernoulli beam theory, see also [10]. If a resonant mode is shifted towards an anti-resonance, the combination of resonance and anti-resonance may be effectively canceled depending on the amount of damping. It is possible to exploit this effect to increase the performance of the system when feedback control is applied for positioning. In such a case the gain peaking and rapid shift in phase associated with the anti-resonance–resonance combination is reduced facilitating the application of simple control systems.

Unfortunately, the assumption that a load is rigid is only reasonable if the frequency range over which the harmonic response is evaluated is limited. The first natural mode of the disk depends on the material properties, the thickness of the disk and the radii of the disk and support. The radius of support is equal to the radius of the piezoelectric tube actuator. For relatively thin loads, the first natural modes of the load may be in the same frequency range as the low order natural modes of the actuator. The harmonic response of the piezoelectric actuator loaded by a flexible disk is shown in Fig. 4. To compare the effect of the load on the dynamics of the actuator, the thickness h_d of the load is varied between 0.76 mm and 1.52 mm. The displacement of the load is evaluated at the center of the disk. If a thin disk is applied, the low order bending modes of the disk will appear in the same frequency range as the low order extension modes of the tube. As a result, the relative ordering of the low order resonant and anti-resonant modes of the thin disk may deviate from the nominal load case (h_d = 1.52 mm) causing a large mismatch in phase between control system and actuator if the control system is tuned for the nominal load case. Ultimately, this may affect the stability of the feedback loop. To illustrate this effect, the three dimensional mode shapes of the first four modes of the actuator in combination with a thin disk is shown in Fig. 5. From this figure it is clear that the mode shape of the second mode is dominated by the bending of the disk. This case corresponds to the case shown as a Coarse-dashed line in Fig. 4. For thicker disks, the low order bending modes appear close to the third and higher order modes in the same frequency range as the radial modes. Modes dominated by radial displacement (see for example Fig. 5, right) are in general hard to control since they tend to appear close together. Therefore, in a practical control design case, the bending modes of the thicker disks (1.52 and 2.28 mm)

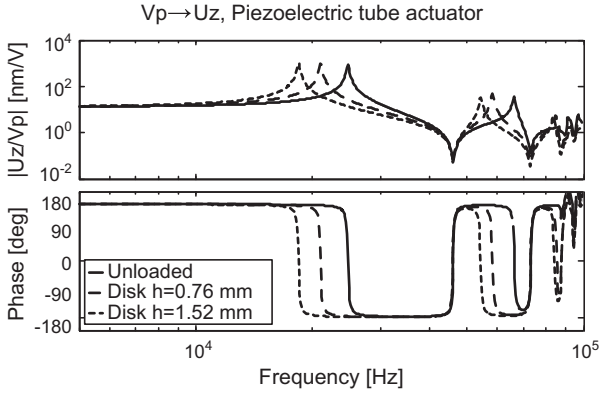

Fig. 3. The dynamics of a piezoelectric tube actuator loaded by a rigid load.

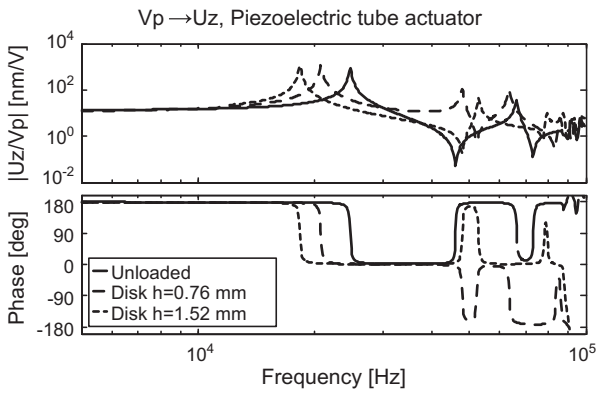

Fig. 4. The dynamics of a piezoelectric tube actuator loaded by a flexible load.

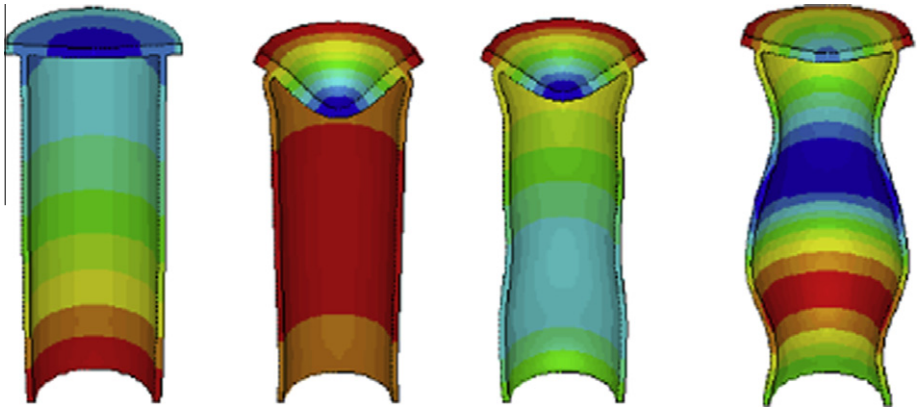

Fig. 5. Three-dimensional mode shapes of the first four modes of the vertical dynamics of the piezoelectric actuator including a thin disk flexible load. The color contours represent deformation in vertical direction.

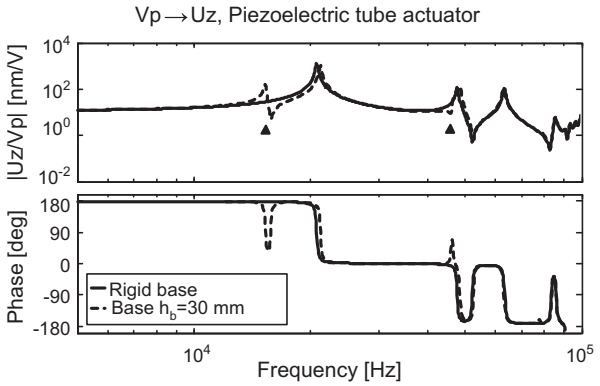

Fig. 6. The dynamics of a piezoelectric tube actuator supported by a flexible mount. The resonant modes introduced by the flexibility of the base are indicated by triangles.

appear in a frequency range where excitation of modes by the control system is avoided by providing roll off.

The dynamics of the piezoelectric actuator are also influenced by the dynamics of a flexible actuator mount. The effect of solid steel base on the dynamics of the tube is shown in Fig. 6. The presence of the base introduces a series of resonant and anti-resonant modes which appear in pairs. This effect occurs due to the fact that the displacement of the fixed end of the actuator is no longer constrained at zero by the rigidity of the base. Additional resonant modes are introduced and anti-resonances occur where two out of phase resonant modes cancel each other out. If the base is very short, a similar effect as the effect of a flexible load occurs. To minimize the influence of the base, the ratio between the length of the base h_b and the length of the actuator L should be as high as possible. The higher this ratio, the closer the introduced resonant modes are to anti-resonant modes, see also Fig. 6.

4. Modal actuation

In systems with poorly damped resonant modes, the harmonic response exhibits large peaks and rapid shifts in phase. These factors complicate the design of a feedback control system if the poorly damped resonant modes occur close to the desired cross-over frequency of the control system. A typical control-based solution to this problem is the application of derivative action to decrease phase lag or notch filtering to reduce the peak-gain, [27]. In contrast, the objective of modal actuation is to shape the harmonic response of the system by avoiding the excitation of a selected set of resonant modes. In the case of piezoelectric actuation, the shaping of the harmonic response may be achieved by modification of the electrodes.

In the approach described by [5], electrode modification was achieved using an etching process. An alternative to shaping electrodes is to divide the electrodes into a number of discrete sections. The total area of the live electrode remains the same and the actuation forces are redistributed by varying the voltages supplied to each section. This method resembles the actuator array approach described in [8,9] but is novel in the sense that the resonant modes of the actuator itself are suppressed instead of the resonant modes of an underlying flexible structure. The advantages of this approach are that suppression of modes may be tuned in situ which enables adaptation to variation in the Eigen frequency of resonant modes. A change in the mechanical load applied to the actuator is a common cause of shifting resonant modes in AFM applications.

A sectioned electrode modal actuator is designed in two steps. In the first step the number and shape of the sections is determined, and in the second step the voltage applied to each section is determined. The number of sections selected for a given actuator is a trade off between several factors such as the number of modes to be suppressed, the number of independent voltage supplies available and for small actuators, the width of the inactive border between sections as well as the influence of the electric wiring and the soldered connections. To determine the voltage levels supplied to the sections, the harmonic response of each section $H_i(\omega)$ is evaluated and an objective in terms of a target harmonic response $H_t(\omega)$ is formulated. The amplitude of the voltages are adjusted according to a set of static gains $g = [g_1,\ldots,g_n]^T$. The gain vector g needed to achieve the objective can be optimized using a constrained least squares optimization which is formulated as:

$$\min_{g\in\mathbb{R}^n} \|H(\omega_0)g - H_t(\omega_0)\|_2, H(\omega_0)\in\mathbb{C}^{n\times m}, H_t(\omega_0)\in\mathbb{C}^m,$$

with $H(\omega_0)$ as the frequency response function matrix, gain set g and objective $H_t(\omega_0)$ defined as:

$$H(\omega_0) = \begin{bmatrix} H_1(\omega_1) & \cdots & H_n(\omega_1) \\ H_1(\omega_2) & \cdots & H_n(\omega_2) \\ \vdots & \ddots & \vdots \\ H_1(\omega_m) & \cdots & H_n(\omega_m) \end{bmatrix},\ g = \begin{bmatrix} g_1 \\ g_2 \\ \vdots \\ g_n \end{bmatrix},\ H_t(\omega_0) = \begin{bmatrix} H_t(\omega_1) \\ H_t(\omega_2) \\ \vdots \\ H_t(\omega_m) \end{bmatrix},$$

where $\omega_0 = \{\omega_1,\ldots,\omega_m\}$ represent a set of frequencies chosen to fit a particular problem. The frequency set may include the natural frequencies of the system but may also include the gain at low frequencies. The constrained least squares problem can be formulated as a set of linear matrix inequalities [28] in the form:

$$\begin{bmatrix} -\gamma & (H(\omega_0)g - H_t(\omega_0))^H \\ H(\omega_0)g - H_t(\omega_0) & -\gamma I \end{bmatrix} < 0,\ g > 0,$$

where $\gamma \in \mathbb{R}$ is the upper bound of $(H(\omega_0)g - H_t(\omega_0))^H(H(\omega_0)g - H_t(\omega_0))$. A solution is obtained by minimizing γ. The constrained $g > 0$ is added to assure that the solution contains only positive gains. This constraint is added to facilitate practical implementation and to preserve static range of the piezoelectric actuator and may be relaxed if the static elongation of the actuator is less important.

In a practical design, the modes of interest are typically the low order resonant modes. In these cases, the objective would be to avoid excitation of resonant modes with Eigen frequencies in the cross over region of the feedback control system. This is reflected in the case study shown in Fig. 7. In this example, a modal actuator based on a 30 mm tube divided in five sections is shown. If all sections are supplied with equal voltages, the response shown in the lower right frame of Fig. 7 is obtained. The optimal gain is calculated for four cases involving the first five modes of the actuator loaded by a flexible disk as shown in Fig. 7 using [29]. The gains are listed in Table 2. The frequency set ω_0 is chosen to match the resonant modes of the first five resonances of the sections shown in Fig. 7. In the first case shown in Fig. 8 (frame 1), the constraint enforcing positive gain sets is relaxed and the modal actuator is tuned to fit the first mode and suppress modes 2–5. This is done by setting the first component of the objective to $H_t(\omega_1) = H_1(\omega_1) + \cdots + H_5(\omega_1)$ and $H_t(\omega_2), \ldots, H_t(\omega_5)$ to zero. In the second case the same objective is set, however in this case the solution is constrained to only positive gains. In the third case the positive gain constraint is enforced but the constraint on mode 3–5 is relaxed. In the forth set Sections 1–3 and Sections 4 and 5 are coupled to form two electrodes. In this case the objective contains only the first and the second mode. The gain sets obtained are summarized in Table 2. The residual error calculated using $(H(\omega_0)g - H_t(\omega_0))^H\ (H(\omega_0)g - H_t(\omega_0))$ indicates that in the cases where the positive gain constraint is enforced, the load case with the thickest disk leads to the lowest error. This indicates that the order in which the resonances and anti-resonances appear has a large influence on the ability to suppress modes when the positive gain constraint is enforced.

In the results shown in Fig. 8, it can be observed that when using set 1 (upper left frame), the static gain of the harmonic response is lower than the response obtained by using set 2 (upper right frame). Also in the nominal load case of set 2 (black, upper right frame), the second mode has not been canceled. It can be concluded that restricting the gains to be positive has a large impact on the results obtained. The load case with the thin flexible disk is the most affected. The reason for this is that the second mode is dominated by deformation of the disk. The mode shape does not resemble a beam type extension mode shape and is therefore not fully orthogonal to the mode shape of the first mode. This problem does not occur in the case with the thicker disks. In these cases the load can be regarded as rigid in the frequency region of interest. In both cases the coupling between radial and axial modes is

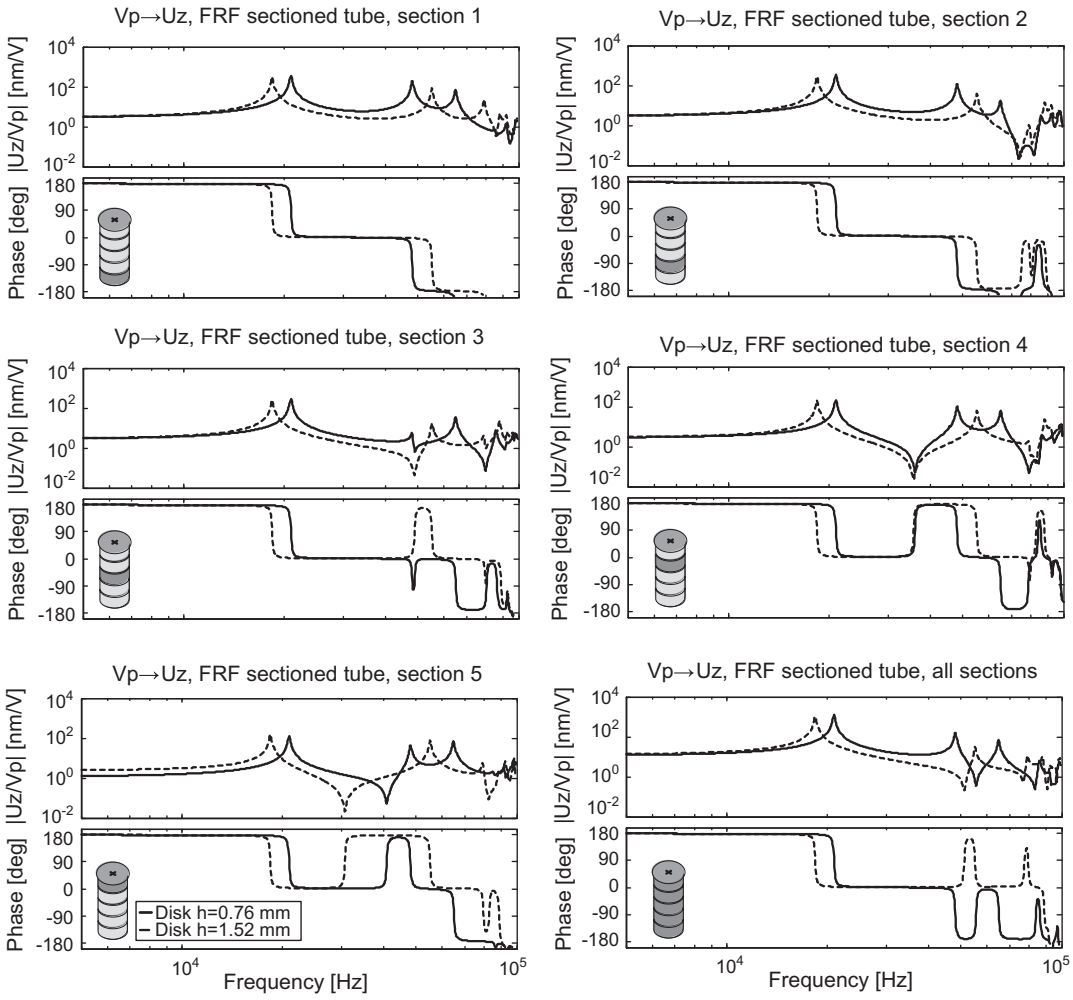

Fig. 7. Harmonic response of a piezoelectric actuator with sectioned electrodes. The actuator is loaded by a steel disk with a 6 mm radius and a thickness of 0.76 mm (solid), 1.52 mm (dashed). The displacement of the load (U_z) is evaluated at the top-center of the disk.

Table 2
Gain set of modal actuation case study.

Set	Case	g_1	g_2	g_3	g_4	g_5
1	1	−0.3198	1.0000	−0.0312	0.8527	−0.8058
	2	0.1395	1.0000	0.4338	0.9771	−0.2691
	3	0.0540	0.6120	1.0000	0.4878	−0.1983
2	1	0.5501	0.3756	0.4293	1.0000	0.2108
	2	0.4413	1.0000	0.5132	0.9249	0.0962
	3	0.3702	0.7552	1.0000	0.5230	0.1767
3	1	0.4647	0.1877	0.1660	1.0000	0.0589
	2	0.4413	1.0000	0.5132	0.9249	0.0962
	3	0.3702	0.7552	1.0000	0.5230	0.1767
4	1	0.4671	0.4671	0.4671	1.0000	1.0000
	2	1.0000	1.0000	1.0000	0.7473	0.7473
	3	1.0000	1.0000	1.0000	0.7505	0.7505

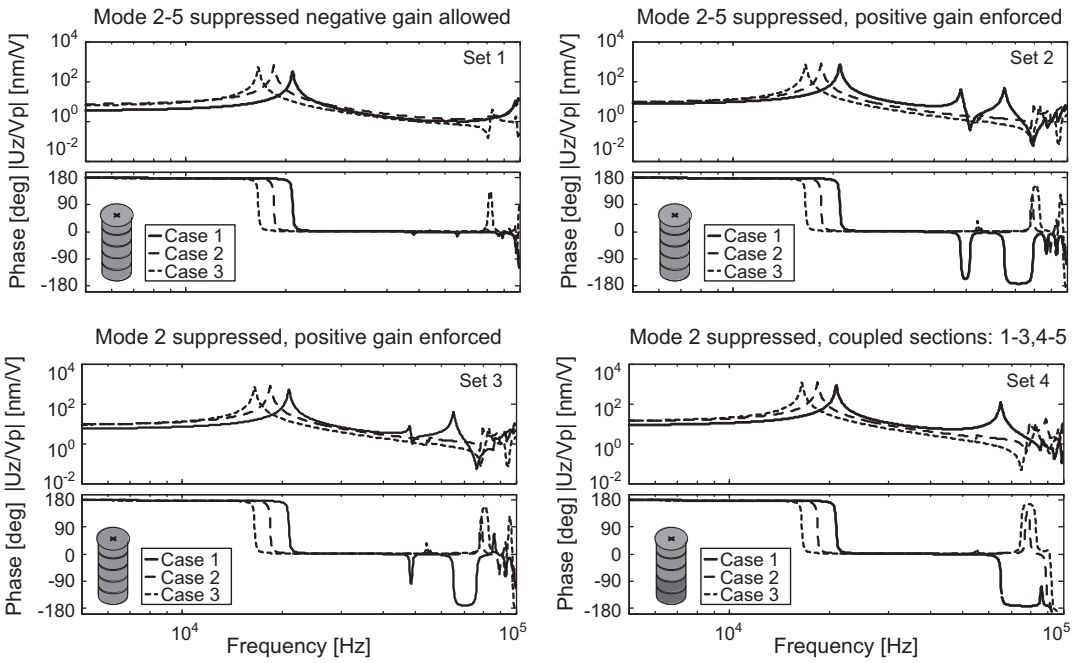

Fig. 8. Modal actuation case study with gain sets based on constrained least squares optimization. The cases shown are: upper-left frame, constraint on positive gain set is relaxed, modal actuator is tuned to fit mode 1 and suppress modes 2–5; upper-right frame, same objective but with a solution constrained to positive gains; lower-left frame, constraint on mode 3–5 is relaxed, but solution is constrained to positive gains; lower-right frame, Sections 1–3 and Sections 4 and 5 are coupled to form two electrodes, the objective contains only the first and the second mode. Cases 1–3 correspond to flexible disks with thickness h_d of 0.76, 1.52 and 2.28 mm.

apparent in the high frequency region (>80) kHz. These modes are difficult to control using load balancing or modal actuation. For this reason a feedback control system needs to provide sufficient roll off in this region to avoid the accidental excitation of these modes.

The harmonic responses plotted in Fig. 7 show that with the nominal load (black) in the case of Sections 4 and 5 there is an anti-resonance between the first two modes which is not present in the case of Sections 1–3. This allows the electric coupling of the first three sections in one group and the last two sections in the second group. Then, by balancing the voltage supplied to both groups, the second mode can be reduced. This is the simplest way to achieve modal actuation with positive voltages which leads to a reduction of the second mode.

5. Limitations to modal control

In high speed designs, the achievable bandwidth can be optimized by the application of relatively short piezoelectric tube actuators which have resonant modes appearing at higher frequencies than those of long tube actuators. A complicating factor in designs based on short tubes is the relative low ratio between length and radius of the piezoelectric tube. As a result, the coupling between the low order radial and axial modes is stronger for short tube actuators.

The low order resonant modes of the vertical axis of the piezoelectric tube actuator behave like Euler–Bernoulli beam extension modes. The radial deformation of the first mode is almost zero and the natural frequency depends strongly on the length of the actuator. In contrast, the radial modes of the piezoelectric tube actuator depend on the radius of the tube and have natural frequencies which are independent of mode number. Coupling between radial and axial modes occurs when the ratio of the length of the actuator and the product of the mode number and the actuator radius is small ($L/(jR) < 8$). The coupling effect is stronger for tubes with thick walls. The coupling between radial and axial modes reduces the frequency spacing of the low order modes. In general, low

order extension modes occur at lower frequencies than those predicted using Euler–Bernoulli beam models. Additional modes appear in the frequency range shared by high order radial modes.

As an example, the first ten radial-axial modes of a short piezoelectric tube ($L \times R = 30 \times 4.75$ mm) are derived using both shell-theory and FEA models. The results are shown in the left frame of Fig. 9. The mode shape of the first mode is shown in the top-right frame of Fig. 9. From this frame it is clear that this mode is almost a pure extension mode. If the radial deformation $w(z,t)$ is assumed to be zero for all z then the model (1) and (2) reduces to that of the axial vibration of an Euler–Bernoulli beam. The natural modes obtained by using this reduced model coincide with the lower modes of the full model and is shown as a dashed line in the left frame of Fig. 9. The higher order radial-axial modes derived by the shell-theory model have a more mixed character, see for example the mode shape of the third mode shown in the right frame of Fig. 9. The natural frequency of this mode is lower than predicted by the reduced model based on Euler–Bernoulli beam theory. If the axial deformation $u(z,t)$ is assumed to be zero then the model (1) and (2) reduces to a shell-theory model describing only radial modes. These modes may be approximated using shell-theory models for shells of infinite length [24]. A good example of such a mode is mode 7, shown in the right frame of Fig. 9. At higher frequencies the modes again resemble Euler–Bernoulli beam type extension modes, see for example the mode shapes of mode 14 shown in the right frame of Fig. 9. It can be concluded that actuators which are short compared to their radius have the advantage that the radial-axial modes occur at higher frequency compared to actuators which are longer but have an increased influence of radial deformation in low order modes.

The radial modes predicted by the shell-theory models for shells of infinite length are not influenced by the mass attached to the free end. In contrast, the axial modes predicted by the Euler–Bernoulli beam model are. Because modes which are close together are inherently difficult to control, the coupling of radial and axial modes may complicate the design of a control system in cases where the load conditions are subject to change. Effective control of these modes using either modal actuation or by load balancing using the boundary conditions is difficult due to the complex nature of the modes and their insensitivity to loading.

6. Experimental verification

Experimental verification of the modal actuation approach was based on a commercially available piezoelectric tube actuator (PT130.20, Physik Instrumente, Karlsruhe, Germany) with a special outer electrode geometry. The outer electrode was separated into five segments with a length of 5.6 mm by circumferential electrode removal. The tube is constructed using PIC151 ceramic. The sectioned tube was excited using a set of five custom piezo amplifiers with a configurable gain.

In Fig. 10 an overview of the experimental setup is presented. The actuator has a length $L = 30$ mm, an inner diameter of $d_i = 9$ mm and an outer diameter $d_o = 10$ mm. The tube is bonded to a steel base with a length of 160 mm using a cyanoacrylate adhesive. To enable experimentation with various loads in the form of standard AFM sample carriers, a magnet is used to hold loads in place. The magnet is bonded to a steel M4 bolt which is connected to the base at the centerline of the actuator. The magnet and the load are in close proximity of each other but not in contact. The clamping force of a neodymium disk magnet with a 6 mm diameter and a thickness of 3 mm can, taking into account a small air gap, produce a force of approximately 4 N [30]. The maximum force required for harmonic motion of the load occurs at the first resonant mode and at the high end of the spectrum. At a drive level of 100 mV and a gain of 1×10^3 nm/V at a frequency of 20 kHz this results in inertial forces of about 2.3 N. The required force is lower for the peaks in at 40 and 60 kHz which require 1 and 0.6 N respectively. In the high frequency range 90–100 kHz the required force increases to a maximum of 5.6 N. The quality of magnetic clamping was verified by repeated measurements using frequency sweeping at different drive levels which show consistent results. The displacement of the load is measured using a capacitive sensor (MicroSense II 6810 with 6504-01 probe, MicroSense LLC, Lowell, Massachusetts, USA). The actuator is loaded using a set of steel ($\rho = 7.8 \times 10^3$ kg/m^3, $E = 200$ GPa) disks with radius $r_d = 6$ mm, thickness $h_d = 0.72$ mm and $h_d = 1.56$ mm. The disks have a mass m_l of 0.64 g and 1.436 g. The piezoelectric tube was excited using a set of up to five independent piezo amplifiers. All electrical connections were soldered using very thin wires to minimize mechanical loading. The inner electrode is electrically connected to the base through a

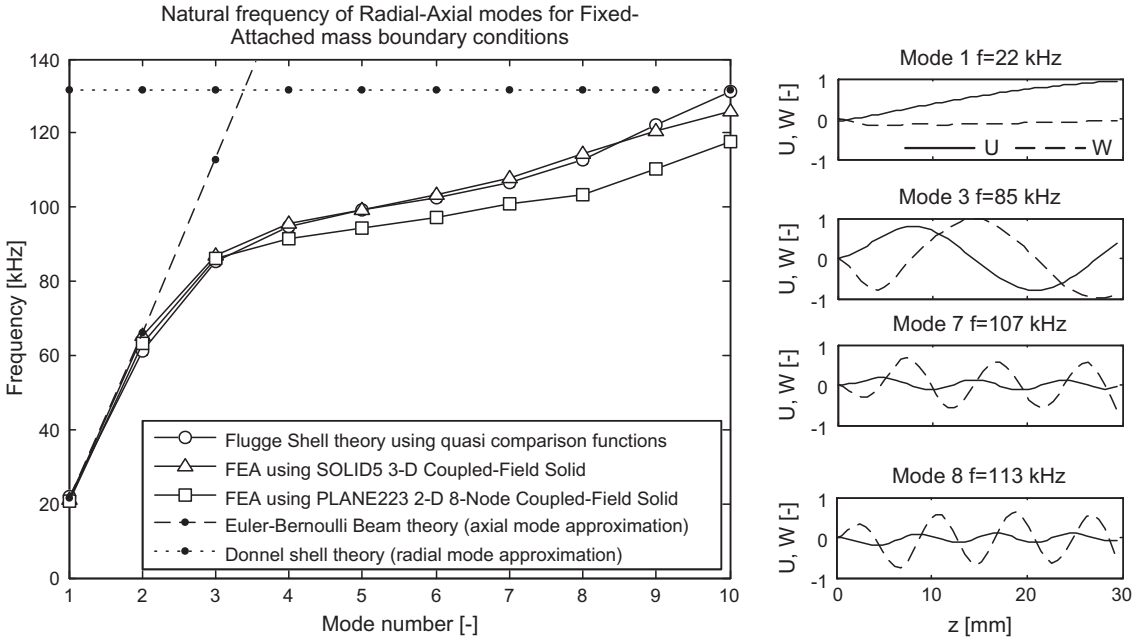

Fig. 9. Natural frequencies of the dominant modes in vertical direction for a piezoelectric tube ($L \times R = 30 \times 4.75$ mm) which is fixed-free including a rigid load.

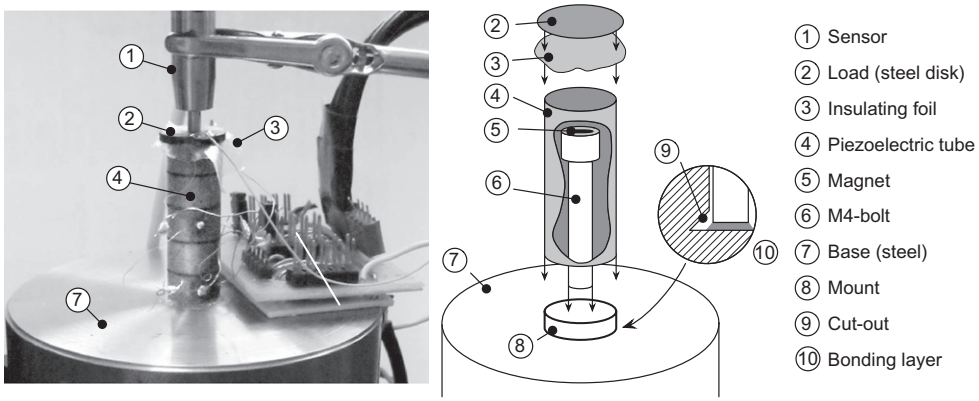

Fig. 10. Experimental setup with modal actuator and capacitive sensor (left) and overview showing the internal components (right).

soldered contact with the metal of the bolt. The electrical resistance is low compared to the output resistance of the amplifiers.

6.1. Dynamics of full tube

The measured response shown in Fig. 11 (lower right frame-black) shows that for the nominal load case (steel disk with radius r of 6 mm and thickness h_d of 0.76 mm) there is a resonant mode at 20, 40 and 60 kHz. When compared with the finite element model with the flexible load shown in Fig. 7 where there are modes at 20, 50 and 65 kHz it is clear that the low order mode matches but the higher order modes are somewhat over-estimated. This may be due to the fact that in the finite element model, the load and the actuator are assumed to be perfectly bonded which increases the stiffness of the system when compared to magnetic clamping. Using magnetic clamping, the deformation of the disk is not counteracted by a bending moment between the free end of the piezoelectric actuator and the load. A more accurate estimation of the low order modes of the disk may be obtained by assuming a simply supported load or by increasing the strength of the bond by using cyanoacrylate adhesive or a larger magnet.

The measured response using the thick disk shown in Fig. 11 (lower right frame in gray) shows that compared to the load case with the thin disk, the second mode and third mode have disappeared. The harmonic response of the model shown in black-dashed in Fig. 7 shows an anti-resonance between the first and the second mode and between second and the third mode. The disappearance of the second and the third mode in the measurement in Fig. 11 (lower right frame-gray) may be due to the proximity of the resonant mode and the presence of damping in the system. The first mode shifts to a frequency of about 18 kHz which is in accordance with the model.

The measurements involving the separate sections shown in frame 1–2 and 4–5 of Fig. 11 show resonant and anti-resonant modes which are in agreement with the modeled harmonic responses shown in Fig. 7. The measurements of the third section are an exception to this rule and show a difference in the order between resonant and anti-resonant modes. This may be due to the difference in bonding between tube and base and tube and load. A dynamical effect not predicted by the shell-theory model are modes which are nearly canceled by anti-resonances. The effect is most apparent as a split peak of the first mode in the case where the actuator is loaded by a thick disk, shown in gray in Fig. 11. The effect may be attributed to the base due to the fact that it is present in the measurement of both load cases.

Although an accurate predicting of the dynamics of the Sections 1 and 2 and Sections 4 and 5 as well as the dynamics of the full tube can be obtained using the model it is not possible to use the model to design a model actuator. The reason for this is the mismatch between model and measured response of the third section. The alternative to model based tuning is tuning using the measured harmonic responses or in situ tuning based on a reduced set of sections.

6.2. Load balancing and modal actuation

The design of a modal actuator can be based on five segments or on a reduced set by combining the segments in groups. The results using either model or measurement based optimization based on five segments did not result in a complete reduction of the targeted modes. The cause of these difficulties may be small differences in phase between the channels. These phase differences may originate in the electrical circuitry or may be the result of material damping. Non-linear behavior of the piezoelectrical actuator itself may also be a factor, although at the low drive levels ($\approx$100 mV) used this is not likely.

For simplicity, the approach shown in frame 4 of Fig. 8 was implemented on the experimental set-up. A set of two independent amplifiers was used to drive the combined sections. Keeping the amplifier of Sections 1–3 constant the voltage level of the second amplifier was lowered until the second mode disappeared. Lowering the voltage level beyond this point caused the mode to reappear. The measured harmonic response at the optimal setting is shown in Fig. 12(left). It is clear that both the peak-gain and the phase shift has been reduced. The measured response also shows that the first resonant mode is unaffected and that the static gain of the system is reduced.

To test the load balancing approach the actuator was loaded by disks of increasing thickness. The measured harmonic response of a the load case with a thick, 1.56 mm disk is shown in gray in Fig. 12(right). The measured response indicates that the application of the thicker load causes the peak gain associated with the second mode to disappear. In addition, the resonant mode introduced by the flexibility of the thin disk is not visible in the increased load case. The results show that in contrast to the modal actuation case the static gain is unaffected and the first mode is shifted to a lower frequency. This disadvantage of the shift of the first mode is offset by the advantage that mode two and three are also reduced. A second advantage of the load balancing approach is its purely mechanical nature. No additional circuitry is needed to deal with non-linear effects such as hysteresis and constitutive non-linearities that may hinder the application of modal actuation using sectioned electrodes at higher drive levels.

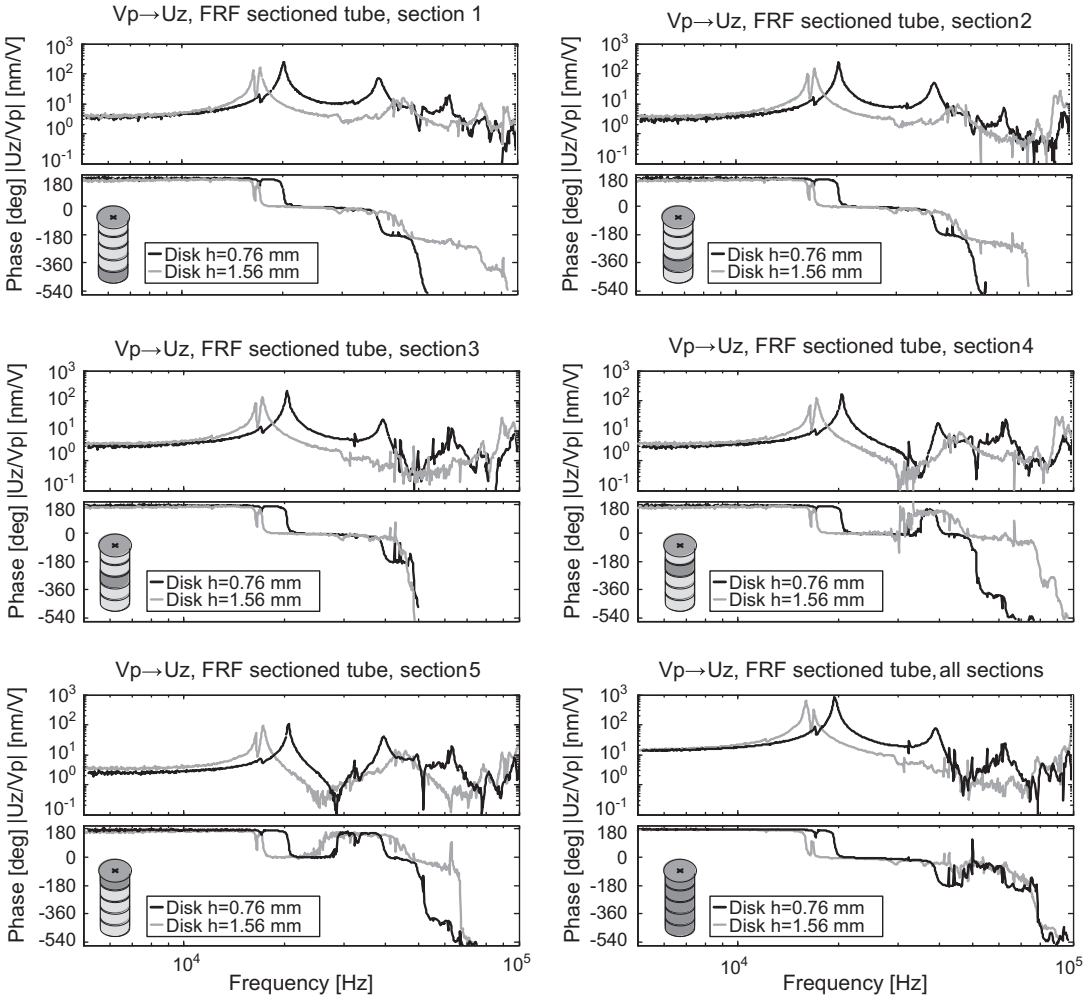

Fig. 11. Measured response of sectioned tube loaded by disks of 0.76 and 1.56 mm.

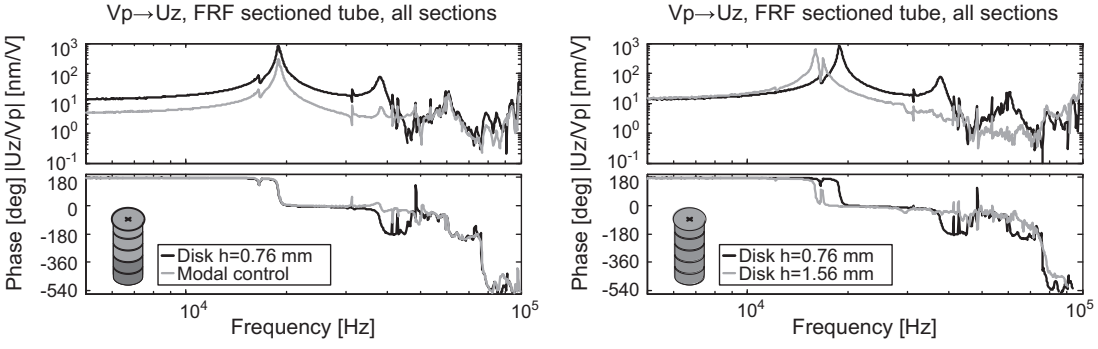

Fig. 12. Measured harmonic response of a modal actuator with gains set for suppression of the second mode (left) compared to an approach where a thick load is applied (right).

7. Concluding remarks

In this paper the implementation of modal actuation on systems actuated by piezoelectric tube scanners has been investigated. It has been shown that the influence of mechanical resonant modes on the dynamics of the system can be reduced by using sectioned electrode modal actuation as well as load balancing. The modal actuation approach can be implemented using a very limited set of sections. If the set is limited to two sections, a single mode may be suppressed using an in situ hand tuning approach. In more elaborate designs, optimization schemes may be employed to tune a modal actuator.

The alternative approach to modal actuation is load balancing where the influence of unwanted resonant modes is reduced by increasing the mass of the applied load. An increased load causes the resonant modes of the system to shift towards lower frequencies. The mass needed to achieve the effect depends on the amount of damping in the system. Systems with relatively high amount of damping require only a small shift in resonant mode and therefore

a small increase in load mass. The application of load balancing has the advantage that compared to modal actuation, the static gain is unaffected. The disadvantage of this approach is that in contrast to modal actuation, the first mode is also shifted towards a lower frequency.

In both cases a reduction in peak gain and phase shift is achieved. This effect may be exploited in the design of a feedback controlled system by facilitating the implementation of simple control schemes over a wider frequency range.

Acknowledgement

This work is part of a project on Model-based subnano-positioning control systems for high-end professional equipment and microsystems manipulation sponsored by the Delft Center for Mechatronics and Microsystems.

References

[1] Binnig G, Quate CF, Gerber C. Atomic force microscope. Phys Rev Lett 1986;56(9):930–3.
[2] Balas MJ. Active control of flexible systems. J Optimiz Theory Appl 1978;25(3):415–36.
[3] Meirovitch L, Baruh H. On the problem of observation spillover in self-adjoint distributed-parameter systems. J Optimiz Theory Appl 1983;39(2):269–91.
[4] Meirovitch L, Baruh H. Control of self-adjoint distributed-parameter systems. J Guid Control 1982;5(1):2053–60.
[5] Lee CK, Moon FC. Modal sensors/actuators. J Appl Mech 1990;57:434.
[6] Preumont A, Franois A, De Man P, Piefort V. Spatial filters in structural control. J Sound Vibr 2003;265(1):61–79.
[7] Preumont A, Franois A, De Man P, Loix N, Henrioulle K. Distributed sensors with piezoelectric films in design of spatial filters for structural control. J Sound Vibr 2005;282(3–5):701–12.
[8] Collins SA, Miller DW, Von Flotow AH. Distributed sensors as spatial filters in active structural control. J Sound Vibr 1994;173(4):471501.
[9] Meirovitch L, Baruh H. The implementation of modal filters for control of structures. J Guid Control Dynam 1985;8(6):707–16.
[10] Adriaens HJMTA, de Koning WL, Banning R. Modelling piezoelectric actuators. IEEE/ASME Trans Mech 2000;5(4):331–41.
[11] Ohara T, Youcef-Toumi K. Dynamics and control of piezotube actuators for subnanometerprecision applications. In: Proceedings of the American control conference, vol. 5; 1995. p. 3808–12.
[12] Tzou HS, Howard RV. A piezothermoelastic thin shell theory applied to active structures. J Vibr Acoust 1994;116:295–302.
[13] Smith RC. Smart material systems: model development. Philadelphia, PA, USA:Society for Industrial and Applied Mathematics.
[14] Maess J, Fleming AJ, Allgöwer F. Simulation of dynamics-coupling in piezoelectric tube scanners by reduced order finite element analysis. Rev Scient Instrum 2008;79(1):015105.
[15] Jahromi SAZ, Salomons M, Sun Q, Wolkow RA. Prediction of the resonant frequency of piezoelectric tube scanners through three-dimensional finite element modeling of a tube assembly. Rev Scient Instrum 2008;79(7):076104.
[16] Flügge W. Stresses in shells. Springer; 1973. ISBN 9780387053226.
[17] Leissa AW. Vibration of shells. NASA-SP-288; 1973.
[18] Reismann H. Forced, axi-symmetric motions of cylindrical shells. J Frank Inst 1967;284(5):308–19.
[19] van Hulzen JR, Schitter G, Van den Hof PMJ, Van Eijk J. Modal actuation for high bandwidth nano-positioning. In: Proceedings of American control conference; 2010. Baltimore, MD, USA. p. 6525–30.
[20] Arnold RN, Warburton GB. Flexural vibrations of the walls of thin cylindrical shells having freely supported ends. Proc R Soc Lond Ser A: Mathe Phys Sci 1949;197(1049):238–56.
[21] Johns DJ, Allwood RJ. Vibration studies of a ring-stiffened circular cylindrical shell. J Sound Vibr 1968;8(1):147–55.
[22] Sharma CB, Johns DJ. Vibration characteristics of a clamped-free and clamped-ring-stiffened circular cylindrical shell. J Sound Vibr 1971;14(4):459–74.
[23] Gartner JR, Olgac N. Improved numerical computation of uniform beam characteristic values and characteristic functions. J Sound Vibr 1982;84(4):481–9.
[24] Blevins R. Formulas for natural frequency and mode shape. Krieger Publishing Company; 2001. ISBN 1-5724-184-6.
[25] Leung AYT. Recurrent integration of beam functions. Comput Struct 1990;37(3):277–82.
[26] ANSYS, Inc. ANSYS Documentation, Release 11.0; 2007.
[27] Abramovitch DY, Andersson SB, Pao LY, Schitter G. A tutorial on the mechanisms, dynamics, and control of atomic force microscopes. In: Proceedings of the American control conference; July 2007.
[28] Boyd S, El Ghaoui L, Feron E, Balakrishnan V. Linear matrix inequalities in system and control theory. SIAM; 1994. ISBN 0-89871-334.
[29] Löfberg J. YALMIP: a toolbox for modeling and optimization in MATLAB. In: Proceedings of the CACSD conference; 2004.
[30] Supermagnete. Webcraft GmbH. Physical magnet datasheet; 2011.